Available online at www.sciencedirect.com
ScienceDirect
Trans. Nonferrous Met. Soc. China 35(2025) 2632−2651
Transactions of Nonferrous Metals Society of China
www.tnmsc.cn

Microstructure, mechanical properties, and bio-corrosion behaviors of Ti-based BCC multi-principal element alloys

Hao-qin LIN[1*], Pan REN[1*], Guang-xu ZHANG[2], Wei-min CHEN[2], Li-jun ZHANG[3]

1. Institute of Advanced Wear & Corrosion Resistant and Functional Materials, Jinan University, Guangzhou 510632, China;
2. Guangdong Provincial Key Laboratory of Metal Toughening Technology and Application, National Engineering Research Center of Powder Metallurgy of Titanium & Rare Metals, Institute of New Materials, Guangdong Academy of Sciences, Guangzhou 510650, China;
3. State Key Laboratory of Powder Metallurgy, Central South University, Changsha 410083, China

Received 24 November 2023; accepted 7 August 2024

Abstract: The equiatomic and equimass TiHfMo, TiHfMoNb and TiHfMoNbZr alloys were prepared, and their microstructure, mechanical properties and bio-corrosion behaviors were systematically investigated. The results demonstrated that all the multi-principal element alloys (MPEAs) had a single BCC phase structure without any intermetallic compounds. Moreover, the Young's moduli and hardness of the MPEAs were respectively within the range of 95−126 GPa and 5.5−6.4 GPa, respectively. In simulated body fluids, the MPEAs had excellent resistance to chloride ion attack due to the fact that the passive films consisted of multiple oxides and the surface possessed large contact angles. Compared with CP-Ti and Ti6Al4V alloy, equiatomic TiHfMo and TiHfMoNb alloys had a desirable combination of pitting and corrosion resistance, wettability, and wear resistance, and can be utilized as potential candidates for biomedical metallic implants.

Key words: multi-principal element alloy; BCC Ti-alloy; microstructure; mechanical properties; bio-corrosion behavior; passive film

---

1 Introduction

With the increase of elderly population around the world, the demand for artificial implants is dramatically increasing [1−3]. Ti and its alloys have developed into a kind of middle-high end surgical implant materials due to the high specific strength, good biological and mechanical compatibility, and easy machining [4,5]. Ti6Al4V alloy is often used for the femoral head replacement market [6]. However, in vivo animal tests reveal that Ti6Al4V alloy releases cytotoxic Al^{3+} and V^{5+} ions due to long-term corrosion, and excessive release of elements Al and V in the human body leads to osteomalacia myopathy, neuropathy, and other symptoms [7]. Moreover, Young's modulus of Ti6Al4V alloy is much larger than that of the cortical bone tissue, resulting in the stress shielding phenomenon and implant loosening [8]. Very recently, various body-centered cubic (BCC) Ti alloys exhibit lower Young's moduli and better biocompatibility compared with Ti6Al4V alloy, providing significant advantages in bone healing and remodeling [9−13]. Therefore, exploring novel Ti-based BCC alloys with excellent properties has

---

* Hao-qin LIN and Pan REN contributed equally to this work

Corresponding author: Wei-min CHEN, Tel: +86-20-87716053, E-mail: chenweiming126@163.com

https://doi.org/10.1016/S1003-6326(25)66837-3

been the focus of biomedical research.

Multi-principal element alloys (MPEAs) including high entropy alloys (HEAs) and middle entropy alloys (MEAs) have a configuration entropy exceeding $0.69R$ (R is the molar gas constant) and are composed of 3 or more elements, breaking the traditional metallurgical boundaries and being widely used in the design of alloys with excellent properties [14,15]. Compared with traditional alloys, MPEAs are typically composed of multiple principal elements with equal or near-equal atomic ratios and are usually a single-phase or multi-phase solid solution [16]. The MPEAs with a single BCC structure usually exhibit high strength and corrosion resistance, which makes them have broad application prospects in many fields [17−19]. In recent years, refractory multi-principal element alloys (RMPEAs) composed of refractory elements such as Ti, Hf, Mo, Nb, Zr and Ta have been developed, which have a single BCC phase [20,21]. Furthermore, owing to the high biocompatibility, the RMPEAs have great potentials for development in the field of biomedical application. Therefore, a series of equimolar and non-equimolar RMPEAs including Ti−Nb−Zr [22], Ti−Zr−(Hf,Ta,Nb) [23], Ti−Zr−Nb−Mo [24,25], Ti−Zr−Hf−Nb [26,27], Ti−Zr−Ta−Hf−Nb [28], Ti−Ta−Nb−Mo−Zr [29] and Mo−Nb−Hf−Zr−Ti [30] alloys have been investigated as biomaterials.

In the existing MPEAs systems for biomedical field, TiHfMo, TiHfMoNb and TiHfMoNbZr alloys with the BCC phase have not been systematically investigated. Based on the aforementioned considerations, these alloys have suitable Young's modulus and good corrosion resistance, and thus are promising as biomedical implants. Therefore, investigations on the microstructure, mechanical properties, and bio-corrosion behaviors of the BCC MPEAs composed of elements Ti, Hf, Mo, Nb and Zr were conducted in this work. Firstly, equiatomic and equimass TiHfMo, TiHfMoNb and TiHfMoNbZr alloys were experimentally prepared and their microstructures were characterized by X-ray diffraction patterns (XRD), optical microscopy (OM), scanning electron microscope (SEM), and electron backscatter diffraction (EBSD). Secondly, mechanical properties of MPEAs were tested by nanoindentation tester to obtain the Young's moduli and hardness. Thirdly, bio-corrosion behaviors of MPEAs in simulated body fluids (SBF) were tested by electrochemical measurements. Finally, passive film and surface wettability of MPEAs were observed by using X-ray photoelectron spectroscopy (XPS) and sessile drop method, respectively. Moreover, CP-Ti and Ti6Al4V alloy were used for comparison in the measurements.

2 Experimental

2.1 Material preparation

The slugs of Ti, Hf, Mo, Nb and Zr with the purity above 99.9 wt.% from Zhongnuo Advanced Material (Beijing) Technology Co., Ltd., were used as raw materials, and the ingots were fabricated by arc melting under an Ar atmosphere using a non-reactive W electrode (WKDHL−1, Opto-electronics Co., Ltd., Beijing, China). The ingots were flipped and re-melted at least six times to improve their homogeneity. The mass of each ingot was about 40 g and the mass loss of ingots before and after arc melting were less than 0.5 wt.%. The samples with the dimension of 10 mm × 10 mm × 3 mm were cut from the ingots through wire electrical discharge machining. Subsequently, the samples ground by using SiC paper were sealed into vacuum quartz tubes, and then solid-solution treated at (1273±2) K for 2 h. Finally, all samples were ground to 2000 grit with SiC paper and then mirror-polished with an alumina polishing solution. Here, samples were denoted as THM1, THM2, THMN1, THMN2, THMNZ1, and THMNZ2, respectively, whose compositions are listed in Table 1.

2.2 Microstructure characterization

XRD was performed by an X-ray diffractometer (D/max−2500/PC, Rigaku Corporation, Japan) equipped with Cu K_α radiation to analyze the phase of the investigated alloys. The scanning spectra were obtained in the range of 20°−90° with a scan rate of 5 (°)/min. OM was used on metallurgical microscope (Axiovert 200 MAT, Carl Zeiss Light Microscope, Germany) to initially observe the microstructural morphology. The samples for OM were mechanically polished through standard metallographic procedures and chemically etched by Kroll's reagent (80% H_2O, 15% HNO_3, and 5% HF in vol.%). A Schottky field emission scanning electron microscope (FE-SEM, JSMIT800, JEOL, Japan) equipped with an EBSD unit was carried out to investigate grain size, structure and orientation.

Table 1 Compositions of MPEAs

Alloy	*x*/%					*w*/%				
	Ti	Hf	Mo	Nb	Zr	Ti	Hf	Mo	Nb	Zr
THM1	33.34	33.33	33.33	−	−	14.86	55.37	29.77	−	−
THM2	56.59	15.18	28.23	−	−	33.34	33.34	33.32	−	−
THMN1	25.00	25.00	25.00	25.00	−	11.53	42.99	23.11	22.37	−
THMN2	43.81	11.76	21.85	22.58	−	25.00	25.00	25.00	25.00	−
THMNZ1	20.00	20.00	20.00	20.00	20.00	9.45	35.25	18.95	18.34	18.01
THMNZ2	35.62	9.55	17.78	18.36	18.69	20.00	20.00	20.00	20.00	20.00

All the samples for EBSD were treated by electropolishing at 30 V and −20 °C for 40 s in a mixed solution (64 vol.% CH_3OH, 30 vol.% $CH_3(CH_2)_3OH$, and 6 vol.% $HClO_4$).

2.3 Mechanical test

Nanoindentation tester (Keysight G200, Agilent Technology, USA) equipped with diamond indenter tip was utilized to obtain the hardness and Young's moduli of samples from the loading and unloading curves by using the Oliver-Pharr analysis. Indentations were carried out in the depth-control mode and the nanoindentation depth was controlled at 1000 nm to avoid depth effects. The hardness and Young's moduli with respective standard deviation were reported as an average of nine valid indentations with the inter-indent distance of 100 μm.

2.4 Electrochemical test

Electrochemical measurements were performed on a typical three-electrode electrochemical cell system, where the sample, platinum electrode and saturated calomel electrode (SCE) were used as working electrode, opposite electrode, and reference electrode, respectively. All the electrochemical tests were conducted in an electrochemical workstation (CHI 760 E, Shanghai Chenhua Instrument Co., Ltd., China) in SBF solution at 37 °C. The ion concentrations (mmol/L) in SBF solution were 142 Na^+, 5.0 K^+, 1.5 Mg^{2+}, 2.5 Ca^{2+}, 4.2 HCO_3^-, 1.0 HPO_4^{2-}, 147.8 Cl^- and 0.5 SO_4^{2-}, which were almost equal to the ion concentration in human plasma. The samples were immersed in SBF solution for 3600 s until the open-circuit potential (OCP) was almost stable. Potentiodynamic polarization analysis was recorded under a scanning rate of 1.0 mV/s from −1 to 1.5 V (vs SCE). The samples under the OCP were subjected to the electrochemical impedance spectroscopy (EIS) and Mott-Schottky (MS) analysis. Then, EIS tests were performed with an amplitude AC voltage of 10 mV and the frequency of 1×10^{-2}−1×10^5 Hz, while MS tests were performed in the voltage range of −1 to 1 V (vs SCE) with an applied frequency of 1 kHz. All electrochemical tests were repeated at least three times to ensure accurate accuracy.

2.5 Surface analysis of passive film

After being immersed in SBF solution for 24 h, the samples were measured by using a spectrometer (K-alpha, Thermo Scientific, United Kingdom) for XPS to analyze the characteristics of the passive films. Here, XPS peaks were calibrated to the standard C 1s binding energy (284.8 eV).

2.6 Measurement of surface contact angle

The surface wettability of samples was carried out by the sessile drop method using a contact angle goniometer (SDC−100S, Dongguan Zhanding precision instrument Co., Ltd., China) at room temperature. At least five measurements were performed by dropping SBF solution upon the surface of each sample. Contact angle represents the average value of five or more drops for each sample.

3 Results and discussion

3.1 Phase analysis and microstructure

The XRD patterns of the MPEAs after annealing at 1273 K for 2 h are shown in Fig. 1(a). The results of XRD patterns confirm that all the

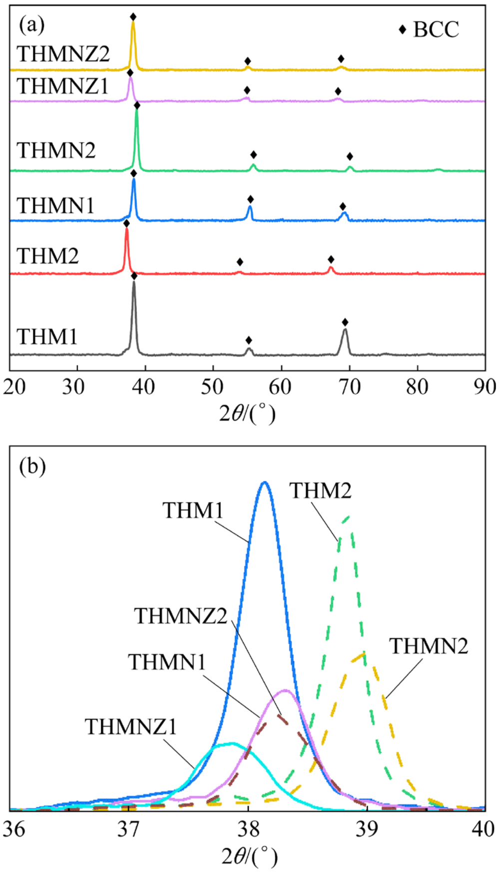

Fig. 1 XRD patterns (a) and magnified main diffraction peaks (b) of MPEAs

solution-treated samples exhibit four strong diffraction peaks of (110), (200), (211) and (220), which refer to a typical BCC crystal structure without any intermetallic compounds. The enlarged figure of the (110) diffraction peak for all the MPEAs is displayed in Fig. 1(b). With the addition of element Nb, the diffraction peak shifts to the right side for the TiHfMo alloy, while the addition of element Zr makes the diffraction peak shift to the left side. This phenomenon is possibly induced by the larger lattice parameter (*a*) of Hf and Zr compared with Ti, Mo and Nb, and the lattice distortion intensity will change significantly by the composition variations. The lattice parameters of Hf and Zr are 355.9 and 358.2 pm, respectively, while the lattice parameters of Ti, Nb and Mo range from 327.6 to 330.3 pm. Besides, the lattice parameters of the MPEAs can be calculated by the Vegard's law ($\alpha=\sum c_i\alpha_i$, where c_i and α_i are the molar fraction and lattice parameter of the *i*th element) [31]. The lattice parameters of THM1 to THMNZ2 alloys are 337.93, 332.66, 335.97, 332.08, 340.42, and 336.96 pm. respectively, and THMNZ1 alloy gets the largest lattice parameter of 340.42 pm. According to the Bragg's law,

$$\alpha=\frac{\lambda\sqrt{h^2+k^2+l^2}}{2\sin\theta} \tag{1}$$

where λ is the wavelength of X-ray radiation, θ is the diffraction angle of the (*hkl*) plane, the larger the lattice parameter, the smaller the diffraction angle of (*hkl*) plane. Therefore, the diffraction peak of (110) of THMNZ1 alloy is smaller than that of other MPEAs.

A criterion for the solid-solution phase formation based on two parameters of δ_r and Ω was proposed to predict phase formation in MPEAs [32,33]. The atomic radius difference δ_r can be used to describe the strength of lattice distortion, which is calculated by

$$\delta_r=\sqrt{\sum_{i=1}^{n}c_i(1-r_i/r)^2}\times100\% \tag{2}$$

where c_i is the atomic fraction of the *i*th component, r_i is the atomic radius of the *i*th atom, and *r* is the average atomic radius) [34].

Parameter Ω is the combined effect of mixing entropy (ΔS_{mix}), mixing enthalpy (ΔH_{mix}), and melting temperature (T_m), which can be expressed as [33]

$$\Omega=\frac{T_m\Delta S_{mix}}{|\Delta H_{mix}|} \tag{3}$$

$\Omega\geq1.1$ and $\delta_r\leq6.6\%$ are required to form solid-solution phases. The thermodynamic parameters and atomic-radius differences of the MPEAs are summarized in Table 2. All the MPEAs can meet the requirements of $\Omega\geq1.1$ and $\delta_r\leq6.6\%$, leading to formation of a stable BCC solid-solution

Table 2 Parameters ΔH_{mix}, δ_r, ΔS_{mix}, Ω, and T_m of MPEAs

Alloy	ΔH_{mix}/(kJ·mol^{-1})	δ_r/%	ΔS_{mix}/(J·K^{-1}·mol^{-1})	Ω	T_m/K
THM1	−3.56	5.99	1.10*R*	6.29	2447.6
THM2	−3.24	4.80	0.97*R*	5.72	2296.4
THMN1	−2.00	5.34	1.39*R*	14.59	2523.3
THMN2	−1.91	4.26	1.28*R*	13.37	2398.8
THMNZ1	−1.60	6.09	1.61*R*	20.44	2444.2
THMNZ2	−1.51	5.58	1.52*R*	19.70	2348.2

phase, which is consistent with the XRD result in Fig. 1(a). Moreover, compared with THM alloy, the addition of Nb decreases the δ_r but increases the Ω, while the addition of Zr increases both δ_r and Ω.

The OM and SEM images of the samples are displayed in Fig. 2. The single-phase BCC solid solution with equiaxed grains is found in the THM1 alloy. However, the other alloys exhibit a dendritic structure, where the typical dendrite (DR) and inter-dendrite (ID) structure can be observed. It can be seen from Table 3 that Hf, Mo, and Nb are partially segregated in the DR region of each MPEA, while Zr is partially segregated in the ID region, which distribute in the residual liquid phase during the solidification of the alloys. Moreover, THM2, THMN2, THMNZ1 and THMNZ2 alloys exhibit high color contrast between the DR and ID regions. These micro-segregations of the components may stem from the difference in element's melting point and mixing enthalpy [35].

Figure 3 shows the inverse pole figure (IPF), grain orientation map, phase map, and grain size distribution of the MPEAs by the EBSD measurements. In Figs. 3(a−f), the results indicate that all the samples have a generally homogeneous microstructure with a similar equiaxial grain structure and orientation. These refractory alloys conform to the Kikuchi line of BCC structure in the inorganic crystal structure database, clearly confirming the existence of the single BCC phase. The average grain sizes of THM2 and THMN2 alloys are 250−300 μm, and those of the other alloys are about less than 250 μm. Compared with the equimass MPEAs, equiatomic MPEAs have smaller average grain sizes, which is caused by the effect of sluggish diffusion [36,37].

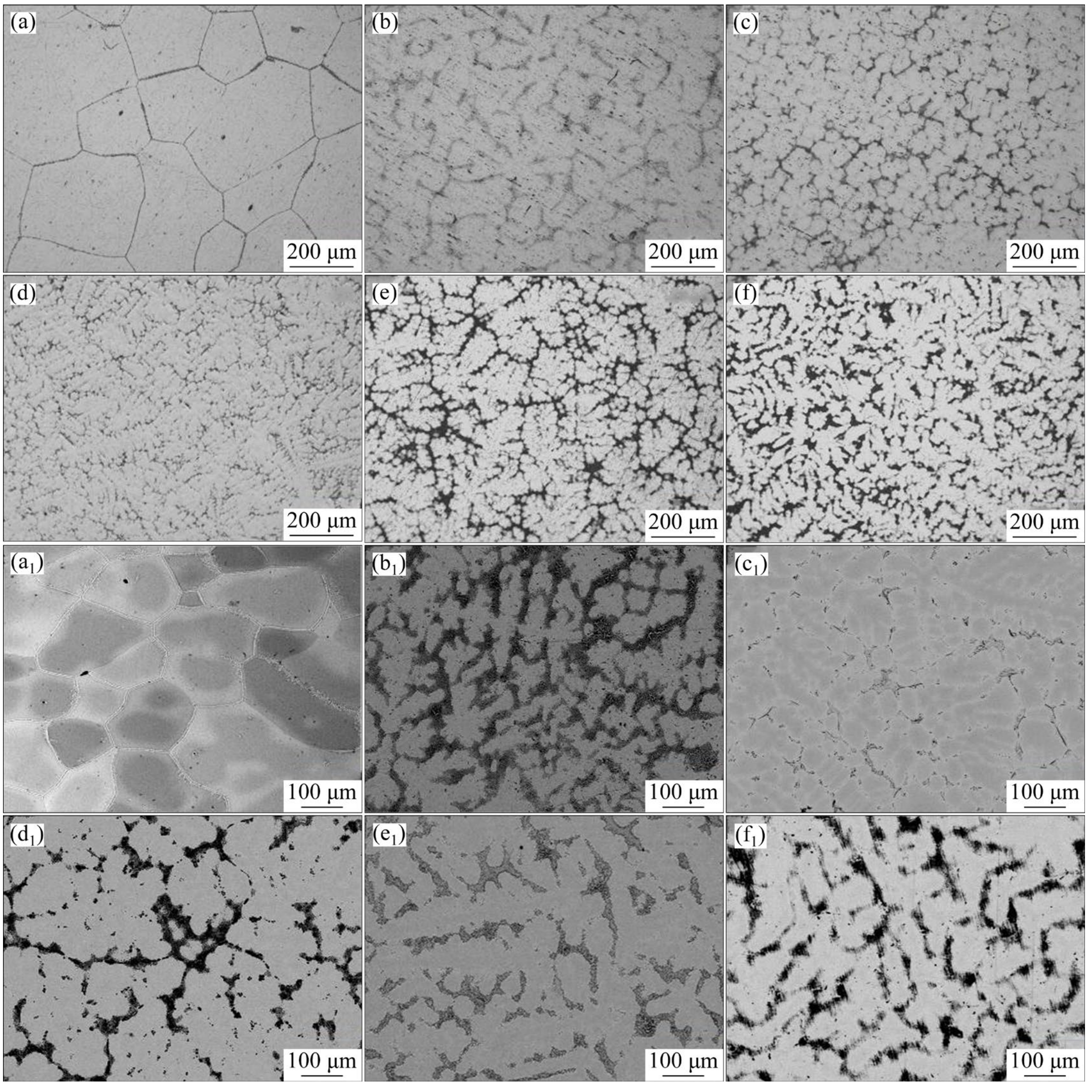

Fig. 2 OM (a−f) and SEM (a_1−f_1) images of THM1 (a, a_1), THM2 (b, b_1), THMN1 (c, c_1), THMN2 (d, d_1), THMNZ1 (e, e_1), and THMNZ2 (f, f_1)

Table 3 Composition of MPEAs by EDS (at.%)

Alloy		Ti	Hf	Mo	Nb	Zr
THM1	Normal	33.34	33.33	33.33	−	−
	DR	32.51	34.11	33.38	−	−
	ID	34.29	33.28	32.43	−	−
THM2	Normal	56.59	15.18	28.23	−	−
	DR	55.49	14.66	29.85	−	−
	ID	56.95	16.34	26.71	−	−
THMN1	Normal	25.00	25.00	25.00	25.00	−
	DR	23.46	24.10	26.46	25.98	−
	ID	24.28	26.95	24.29	24.48	−
THMN2	Normal	43.81	11.76	21.85	22.58	−
	DR	44.39	10.24	22.55	22.82	−
	ID	45.17	13.05	20.82	20.96	−
THMNZ1	Normal	20.00	20.00	20.00	20.00	20.00
	DR	18.65	21.13	20.15	20.86	19.21
	ID	19.44	20.92	18.52	18.98	22.14
THMNZ2	Normal	35.62	9.55	17.78	18.36	18.69
	DR	35.78	10.02	17.29	18.92	17.99
	ID	36.33	10.44	15.38	15.46	22.39

3.2 Mechanical properties

Nanoindentation tests were performed on the MPEAs to obtain the corresponding Young's moduli and hardness. All the results are listed in Table 4. It can be found that the hardness (*H*) and Young's moduli (*E*) of the MPEAs are within the range of 5.5−6.4 GPa and 95.6−126.2 GPa, respectively. Compared with the equiatomic MPEAs, equimass MPEAs have lower Young's moduli, indicating that the rich-Ti alloys have lower Young's moduli, and the addition of Nb and Zr can also reduce the Young's moduli of the alloys. Moreover, according to the wear theory [38], wear resistance can be represented by using the ratios of hardness to Young's modulus including H/E and H^3/E^2, which separately symbol the ability to resist elastic strain to failure and the materials' resistance to plastic deformation in loaded contact, respectively. In Ref. [9], the values 0.04 and 0.009 are recommended as the reference data of H/E and H^3/E^2 for comparison, and the Ti alloys with the higher H/E and H^3/E^2 values exhibit good wear resistance. In this study, the experimental results reveal that the ratios of H/E and H^3/E^2 for the MPEAs are larger than 0.04 and 0.009, enabling better wear resistance.

Table 4 Mechanical properties of MPEAs by nano-indentation test

Alloy	*H*/GPa	*E*/GPa	*H*/*E*	(H^3/E^2)/GPa
THM1	6.39±0.09	126.22±3.32	0.051	0.016
THM2	6.20±0.18	105.83±3.41	0.059	0.021
THMN1	5.52±0.10	119.98±3.37	0.046	0.012
THMN2	6.17±0.05	103.29±2.36	0.060	0.022
THMNZ1	5.53±0.10	99.13±1.89	0.056	0.017
THMNZ2	5.83±0.28	95.61±2.62	0.061	0.022

3.3 Potentiodynamic polarization behavior in SBF

The potentiodynamic polarization curves of all the MPEAs and two reference materials including CP-Ti and Ti6Al4V were measured in SBF solution at a scanning rate of 1 mV/s, which are shown in Fig. 4(a). It can be seen that the current density decreases and then increases as the potential changes from negative to positive values, and the anode curve appears a relatively stable and wide passivation zone. In this passivation zone, the potential increases but the current density remains relatively stable, indicating the self-passivation characteristics of all the samples. Moreover, the electrochemical parameters such as corrosion potential (φ_{corr}), complete passivation potential (φ_{cp}), corrosion current density (J_{corr}), and passivation current density (J_{pass}) can be obtained from the Tafel plot, and the results are listed in Table 5.

It is found that the THM1 alloy exhibits the highest φ_{corr} of −0.244 V and the lowest J_{corr} of 0.067 $\mu\mathrm{A{\cdot}cm^{-2}}$, whereas the THMN2 alloy exhibits lower φ_{corr} of −0.365 V and the highest J_{corr} of 0.143 $\mu\mathrm{A{\cdot}cm^{-2}}$. This result may be caused by the recrystallization of the THM1 alloy after annealing, the formation of fine equiaxed grains, and the disappearance of the inhomogeneity of the structure. Besides, the THM1, THMN1 and THMNZ2 alloys have lower J_{corr} than CP-Ti, indicating higher corrosion resistance. It should be noted that THM2 and THMN2 alloys have relatively high J_{pass}, which is the coarse grains formed in the alloy significantly reduce the nucleation site of the passive film, and the passivation first occurs on surface crystalline

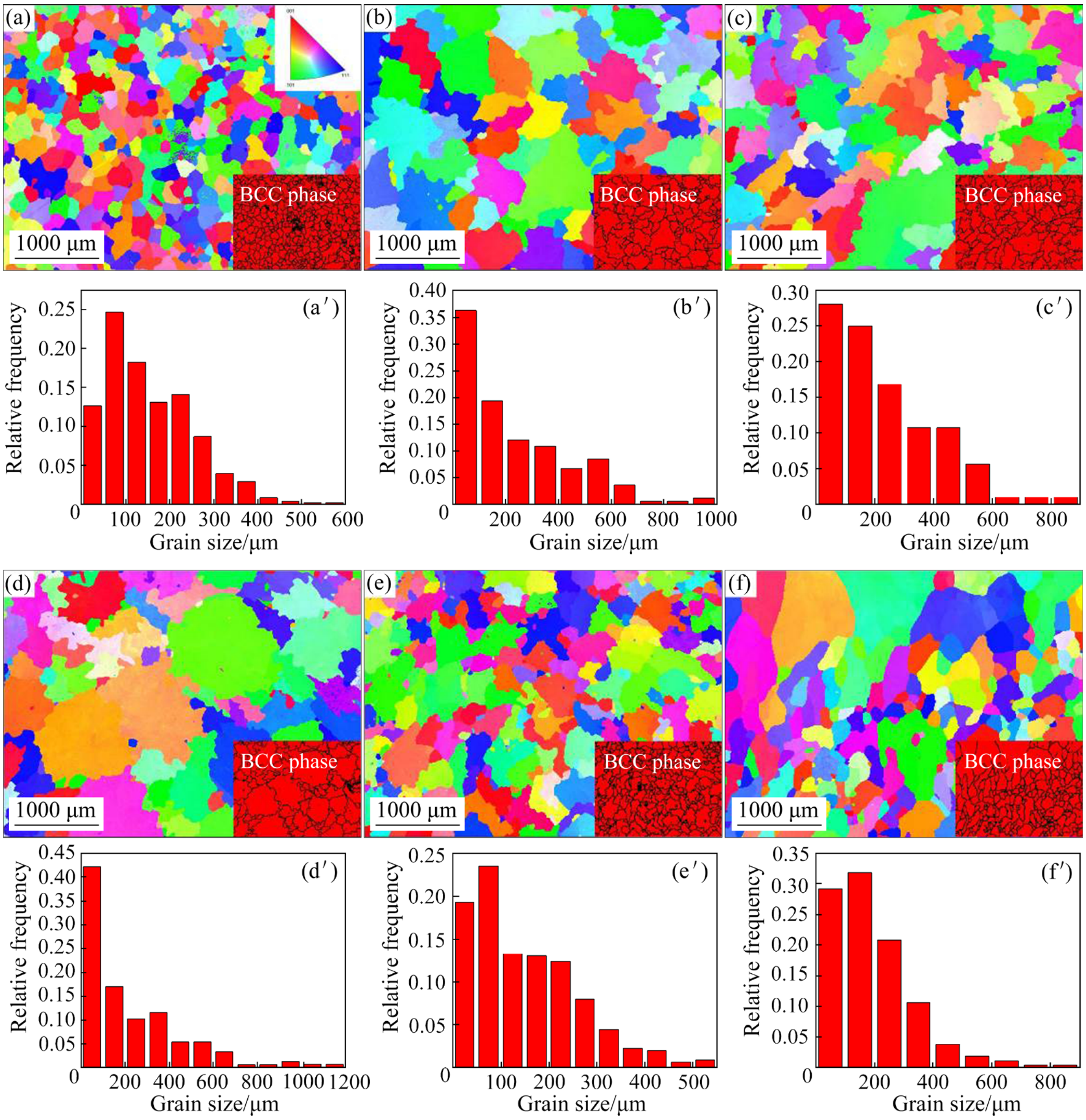

Fig. 3 EBSD IPF maps (a−f) and corresponding grain size distributions (a′−f′) of MPEAs: (a, a′) THM1; (b, b′) THM2; (c, c′) THMN1; (d, d′) THMN2; (e, e′) THMNZ1; (f, f′) THMNZ2

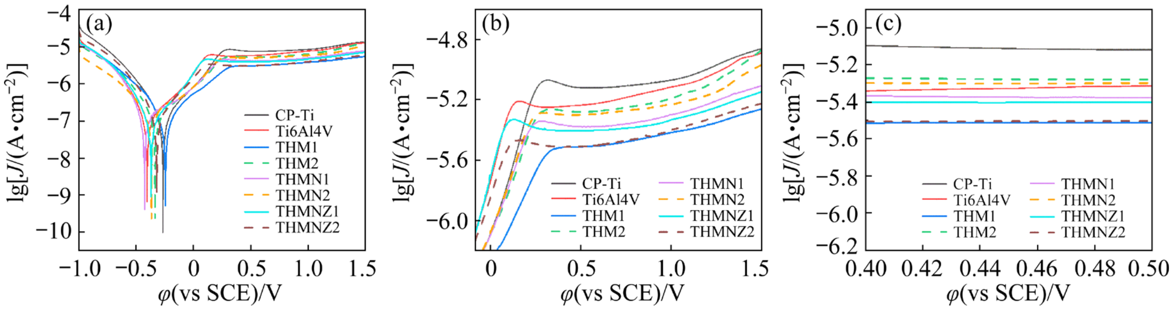

Fig. 4 (a) Potentiodynamic polarization curves of samples tested in SBF solution; (b) Passivation zone of potentiodynamic polarization curve; (c) Current density variations at 400−500 mV in SBF solution

lattice defects of Ti [39]. Therefore, grain refinement can improve the corrosion resistance of alloys with the thick, dense, and homogeneous amorphous film [39,40]. Furthermore, it can be found that all the MPEAs have lower J_{pass} than CP-Ti, which may be attributed to the passivation effect of Nb, Hf and Mo on Ti alloys. Similarly, the φ_{cp} of CP-Ti is higher than those of MPEAs except THM1 alloy, which indicates an easy tendency of MPEAs to be passivated. Additionally, it is clearly seen from Fig. 4(b) that all the MPEAs exhibit extensive passivation on the polarization curve without pitting, indicating that the passive film has a high resistance to Cl^- ions attack. The current density is determined for the characterization of the corrosion activity of the materials. Thus, the current density variations at 400−500 mV in SBF solution, corresponding to the ion release of the biomaterial in the surrounding tissue under physiological conditions [41], are shown in Fig. 4(c). Compared with CP-Ti, all the MPEAs have lower current density under physiological conditions and lower release rate of metal ions, which can reduce the occurrence of chronic inflammation around the implant.

3.4 Electrochemical behaviors

Figure 5 illustrates the electrochemical impedance spectroscopy (EIS) spectra of the samples tested in SBF solution. All of the samples have a similar feature of an unfinished semi-arc in the Nyquist plots (Fig. 5(a)). The radius of the capacitor arc, which represents the polarization resistance of the passive film, differed among the samples. Accordingly, the corrosion characteristics of the samples in the frequency range are given in Bode plots (Figs. 5(b, c)). In the high frequency range of 10^3−10^5 Hz, the impedance of the samples is small in the range of 10−100 $\Omega\cdot cm^2$, and the phase angle remains almost constant around 0°. These results indicate that the resistivity of the electrolyte is negligible. In the middle and low frequency range of 10^{-2}–10^3 Hz, the slope of the Bode impedance spectra of all the samples is close to −1, reflecting the superior corrosion resistant performance of the passive film formed on the samples. Moreover, the relatively stabilized phase angles (70°−80°) can be distinguished in the same frequency range of 10^{-2}−10^3 Hz for CP-Ti, Ti6Al4V, THM1, THMN1, and THMNZ2 alloys, while 10^{-1}−10^3 Hz for THM2, THMN2, and THMNZ1 alloys, indicating a capacitive response related to the presence of passive film. Based on the above results, the large phase angle in the Bode plots indicates that at least two time constants interact with each other. According to Ref. [42], these characteristics may be caused by the double-layer passive film structure formed on the surface of the

Table 5 Electrochemical parameters of samples after polarization in SBF solution

Alloy	φ_{corr}(vs SCE)/V	φ_{cp}(vs SCE)/V	$J_{corr}/(\mu A\cdot cm^{-2})$	$J_{pass}/(\mu A\cdot cm^{-2})$
CP-Ti	−0.265±0.012	0.317±0.011	0.093±0.011	7.586±0.452
Ti6Al4V	−0.404±0.019	0.147±0.008	0.090±0.013	4.227±0.102
THM1	−0.244±0.018	0.336±0.021	0.067±0.003	3.069±0.251
THM2	−0.334±0.019	0.302±0.015	0.127±0.007	5.458±0.342
THMN1	−0.425±0.021	0.254±0.017	0.089±0.005	4.539±0.431
THMN2	−0.365±0.035	0.265±0.006	0.143±0.015	5.081±0.122
THMNZ1	−0.369±0.029	0.113±0.023	0.106±0.009	3.954±0.271
THMNZ2	−0.318±0.031	0.128±0.011	0.091±0.006	3.119±0.167

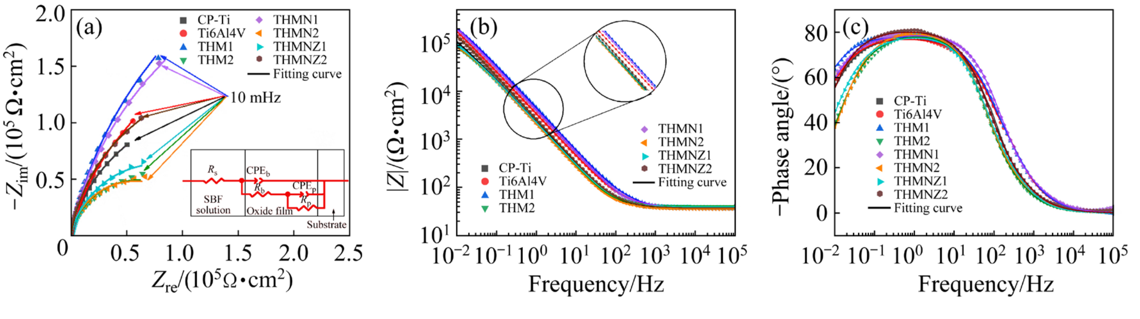

Fig. 5 EIS spectra of samples tested in SBF solution: (a) Nyquist plots; (b) Bode magnitude plot; (c) Bode phase plot

samples. In the double-layer passive film structure of Ti alloys, the outer layer is composed of a porous microstructure in contact with solution, whilst the inner layer barrier in contact with the metal surface acts as a compact barrier.

To quantify the difference in physical−chemical behaviors of CP-Ti, Ti6Al4V and all the MPEAs, the equivalent circuit ($R_s[Q_p(R_p(Q_bR_b))]$) with two time constants was employed to fit the EIS data in Fig. 5. The circuits consist of electrolyte resistance (R_s), porous outer layer resistance (R_p), dense inner layer resistance (R_b), and capacitances of the outer porous layer and inner compact layer ($\mathrm{CPE_p}$ and $\mathrm{CPE_b}$). In this study, a constant phase element (CPE) was chosen instead of a capacitor (C) as the distribution of relaxation time due to the fact that the electrode surface heterogeneity is related to the charge transfer capacity and capacitance of the metal−electrolyte interface passive film. The impedance of CPE (Z_{CPE}) is defined as

$$Q=Z_{\mathrm{CPE}}=[Y_0(\mathrm{j}\omega)^n]^{-1} \tag{4}$$

where Y_0 is the scale factor, j is the imaginary unit, ω is the angular frequency, and n is the exponent of CPE related to surface inhomogeneity, with values ranging from −1 to 1. The values of CPE, n, R_p and R_b are obtained and shown in Table 6. The Chi-squared (χ^2) values of all investigated samples are in the order of 10^{-4}, which indicates the nice agreement between the experimental data and fitting results.

It can be found that each sample has a high R_b, and the R_b is about 10^3 order of magnitude higher than the R_p. Therefore, the corrosion resistance of the samples mainly depends on the inner dense layer, while the outer loose layer makes a small contribution to corrosion resistance. The n values of the films formed on the surface of the samples are in the range of 0.8297−1.000, indicating that the CPEs are essentially non-ideal capacitances. The effective capacitance (C_{eff}) can be obtained from the fitted CPE [43]:

$$C_{\mathrm{eff}}=\mathrm{CPE}(f_{\mathrm{m}})^{n-1} \tag{5}$$

where f_{m} represents the frequency that the imaginary part of the impedance (Z_{img}) reaches its maximum value (see Fig. 5(a)). $C_{\mathrm{eff\text{-}p}}$ and $C_{\mathrm{eff\text{-}b}}$ represent the effective capacitance of the outer porous layer and inner compact layer, respectively. The R_b and $C_{\mathrm{eff\text{-}b}}$ reflect the corrosion resistance of the samples, respectively. The larger the R_b is, the smaller the $C_{\mathrm{eff\text{-}b}}$ is, further leading to the sample with better corrosion resistance. It can be found that THM1 alloy has the largest R_b of $6.945\times10^5\ \Omega\cdot\mathrm{cm}^2$ and the smallest $C_{\mathrm{eff\text{-}b}}$ of $3.379\times10^{-5}\ \mathrm{F\cdot cm^2}$, whereas THMN2 alloy has the smallest R_b of $1.149\times10^5\ \Omega\cdot\mathrm{cm}^2$ and the largest $C_{\mathrm{eff\text{-}b}}$ of $14.767\times10^{-5}\ \mathrm{F\cdot cm^2}$. This result for THMN2 alloy may be caused by the large BCC phase boundary in the alloy which leads to a decrease in the number of oxygen diffusion channels, and further results in poor density of the passive film. Besides, The $C_{\mathrm{eff\text{-}p}}$ is lower than $C_{\mathrm{eff\text{-}b}}$ of THM2, THMN2, and THMNZ1 alloys, which might be attributed to a defective inner layer that leads to the development of a thicker, more porous outer layer. Furthermore, THM1 and THMN1 alloys have higher R_b and lower $C_{\mathrm{eff\text{-}b}}$ than CP-Ti and Ti6Al4V alloy. According to the total impedance of the alloys and the results in Table 6, the corrosion resistance of the tested samples is arranged in order: THM1 > THMN1 > Ti6Al4V > THMNZ2 > CP-Ti > THMNZ1 > THM2 > THMN2, which is in good agreement with the result from potentiodynamic polarization curves.

Table 6 C_{eff} and fitting data designated from EIS measurements of tested alloys in SBF solution

Alloy	R_s/ $(\Omega\cdot\mathrm{cm}^2)$	$\mathrm{CPE_P}$/ $(10^{-5}\ \mathrm{s}^n\cdot\Omega\cdot\mathrm{cm}^2)$	$C_{\mathrm{eff\text{-}P}}$/ $(10^{-5}\ \mathrm{F\cdot cm^2})$	n_1	R_P/ $(10^2\ \Omega\cdot\mathrm{cm}^2)$	$\mathrm{CPE_b}$/ $(10^{-5}\ \mathrm{s}^n\cdot\Omega\cdot\mathrm{cm}^2)$	$C_{\mathrm{eff\text{-}b}}$/ $(10^{-5}\ \mathrm{F\cdot cm^2})$	n_2	R_b/ $(10^5\ \Omega\cdot\mathrm{cm}^2)$	χ^2/ 10^{-4}
CP-Ti	37.07	6.790	11.664	0.8827	0.423	5.748	10.498	0.8692	3.003	2.62
Ti6Al4V	37.32	6.021	12.379	0.8435	0.886	3.288	5.804	0.8766	4.201	3.62
THM1	37.55	4.104	7.112	0.8806	1.279	1.775	3.379	0.8602	6.945	2.17
THM2	38.62	4.126	6.016	0.9181	0.326	6.448	13.985	0.8319	1.219	4.62
THMN1	38.07	4.533	8.352	0.8673	1.012	3.238	5.578	0.8819	5.947	8.27
THMN2	38.47	3.506	5.327	0.9656	0.307	7.746	14.767	0.8599	1.149	2.31
THMNZ1	39.78	5.406	5.406	1.000	0.348	6.561	11.914	0.8297	1.594	1.98
THMNZ2	37.91	3.871	6.421	0.8901	0.454	3.413	6.131	0.8728	3.345	1.32

3.5 Mott-Schottky analysis

In general, the compositions and structures of the passive films have important effects on the corrosion resistance. To further investigate the structure of the passive film of samples, MS technique was used to measure the semiconducting properties of the passive film in SBF solution from the φ(vs SCE) value of −1 to 1 V. The semiconductor type of the passive film can be determined by the MS curve slope. The positive slope represents the n-type semiconductor characteristics, and the negative slope represents the p-type semiconductor characteristics. Figure 6 illustrates the MS curves of CP-Ti, Ti6Al4V, and MPEAs. It is seen from the figure that all the characterized samples show positive slopes in SBF solution, which conforms to the property of n-type semi-conductor. Thus, the dominant defects in the oxide layer are donors, such as oxygen vacancies or titanium interstitials. For n-type semi-conductor, the semiconductor properties of passive films are given by the following relation [44]:

$$\frac{1}{C}=\frac{2}{\varepsilon_0\varepsilon_r eN_D}(\varphi-\varphi_{FB}-\frac{kT}{e}) \tag{6}$$

where ε_r represents the dielectric constant of the passive films, ε_0 represents the vacuum permittivity (8.854×10^{-14} F/cm), e represents the elementary charge (1.602×10^{-19} C), N_D represents the donor concentration, φ represents the applied potential, φ_{FB} represents the flat band potential, k represents the Boltzmann constant (1.38×10^{-23} J/K), and T represents the thermodynamic temperature. The kT/e term can be ignored because the value is about 25 mV at room temperature. The approximate ε_r values of Ti, Hf, Mo, Nb and Zr oxides in the passive films are 60, 25, 29, 41 and 51, respectively, ignoring the difference among various high-priced oxides and oxides of Ti, Mo and Nb [45−47]. Thus, the values of the dielectric constant of the passive films are given by the logarithmic composition and mixture rule [48]:

$$\ln \varepsilon_r=\sum V_i \ln \varepsilon_i \tag{7}$$

where V_i is the volume fraction, and ε_i is the dielectric constant of the component oxide. The ε_r and N_D are listed in Table 7. The results show that the N_D values from the slope by fitting the linear part are 0.71×10^{20}, 0.51×10^{20} and $(0.51−2.75)\times10^{20}$ cm^{-3} for CP-Ti, Ti6Al4V and MPEAs, which are within the reasonable range of 1×10^{18}–1×10^{23} cm^{-3}. The higher N_D values indicate higher chemical affinity for chloride ions than hydroxyl groups, which is detrimental to the passive film and impaired their barrier properties [49]. Therefore, THM1 alloy has the lowest N_D of 0.51×10^{20} cm^{-3} among all the samples, and the THMN1 (0.69×10^{20} cm^{-3}) and THMNZ2 (0.88×10^{20} cm^{-3}) alloys also have lower N_D compared with the other MPEAs, indicating that they generate denser passive films with better corrosion resistance, which is consistent with the potentiodynamic polarization results in Fig. 4.

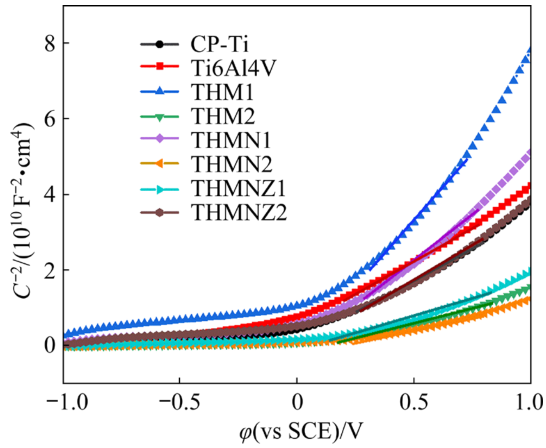

Fig. 6 MS curves of samples tested in SBF solution

Table 7 ε_r and N_D for passive film on CP-Ti, Ti6Al4V and MPEAs in SBF solution at 37 °C

Alloy	ε_r	Slope/ (10^{10} cm^4·F^{-2}·V^{-1})	N_D/ 10^{20} cm^{-3}
CP-Ti	60	3.34	0.71
Ti6Al4V	60	4.22	0.56
THM1	35	7.96	0.51
THM2	43	1.59	2.06
THMN1	36	5.67	0.69
THMN2	42	1.22	2.75
THMNZ1	41	1.87	1.84
THMNZ2	45	3.55	0.88

The thickness (D_{eff}) of the passive film can be evaluated in combination with the numerical values of C_{eff} in Table 6 by [50]

$$D_{eff}=\frac{\varepsilon_r\varepsilon_0}{C_{eff}} \tag{8}$$

Combined with the calculated C_{eff}, the thicknesses of the passive film of CP-Ti, Ti6Al4V, THM1, THM2, THMN1, THMN2, THMNZ1 and THMNZ2 alloys are estimated to be 0.95, 1.33, 1.36, 0.90, 0.97, 0.94, 0.98 and 1.27 nm, respectively. Thus, the THM1 alloy has the best corrosion resistance and the highest passivation film stability among the alloys. It should be noted that the results are slightly different from those obtained by potentiodynamic polarization results, which is caused by the oxide composition of the double-layer passive film on the surface.

3.6 XPS analysis of passive film

After biomedical-Ti alloy is implanted into human body, the passive film generated on its surface plays a key role in the corrosion resistance of the implant in the complex environment of human body. To investigate the passivation behavior of the MPEAs, XPS analysis was performed to elucidate the composition of the passive film after all the samples were soaked for 24 h to obtain the stable OCP. Figure 7 illustrates the high-resolution XPS spectra of the constituent elements. It exhibits the characteristic peaks of C 1s, O 1s, Ti 2p, Hf 4f, Mo 3d, Nb 3d and Zr 3d. The C 1s peak is attributed to the unavoidable contamination of hydrocarbon on the top surface of the samples.

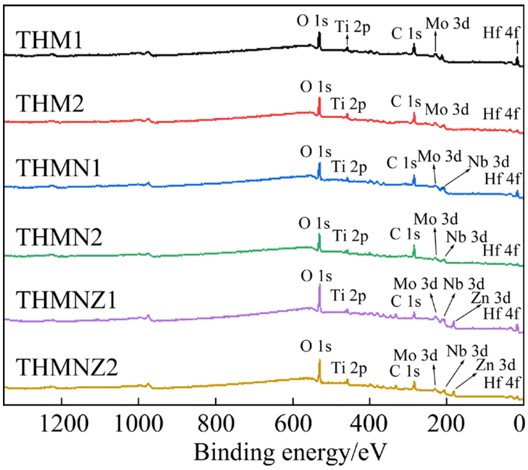

Fig. 7 Survey XPS spectra of alloys after being immersed in SBF solution for 24 h

Figure 8 shows the high-resolution XPS spectra of the Ti 2p, Hf 4f, Mo 3d, Nb 3d and Zr 3d after the MPEAs are immersed in SBF solution for 24 h. All the results are fitted against the NIST XPS database. For the Ti element, Figs. 8(a_1−a_3) present the high-resolution Ti 2p spectra of the MPEAs. Ti $2p_{1/2}$ and Ti $2p_{3/2}$ peaks are found at 464.0−464.2 and 458.2−458.4 eV for the Ti^{4+}, respectively. For Ti^{3+} and Ti^{2+}, Ti $2p_{3/2}$ peaks are respectively observed at 456.9−457.4 and 455.3− 455.6 eV, and the peaks of Ti^0 (located at 453.3− 453.7 eV) are also observed. Therefore, Ti oxides formed in the passive film of the MPEAs are mainly TiO_2, Ti_2O_3, and TiO. For Hf, only Hf^{4+} and Hf^0 are found in the passive films, indicating that only HfO_2 is generated in all the MPEAs, as shown in Figs. 8(b_1−b_3). For the Mo oxide, the formed passive films are composed of MoO_3 and MoO_2, which can be found from the high-resolution Mo 3d spectra of the MPEAs in Figs. 8(c_1−c_3). It can be found that the relative content of Mo in the MPEAs is relatively high, which indicates that Mo has weak oxidation capacity at the reaction interface.

For the THMN1, THMN2, THMNZ1, and THMNZ2 alloys, stable Nb oxides will be formed from the following sequence of consecutive oxidation reactions:

$$Nb+H_2O=NbO+2H^++2e \tag{9}$$

$$NbO+H_2O=NbO_2+2H^++2e \tag{10}$$

$$NbO_2+H_2O=Nb_2O_5+2H^++2e \tag{11}$$

It can be found that there are many forms of Nb in the passive film, and the main form of Nb in the passive film is Nb_2O_5. Small amounts of NbO_2 or NbO, and metal Nb are also presented in Figs. 9(a, b). In addition, no NbO_2 is detected in the passive film of THMN2 alloy. A possible reason for this phenomenon will be given later in this study. Similar to the Hf element, Fig. 9(c) shows the coexistence of Zr^{4+} and Zr^0 in the passive film of the THMNZ1 and THMNZ2 alloys, and no other low valence oxides are found. These results indicate that Zr has a high oxidation capacity at the reaction interface.

As shown in Figs. 10(a−c), the O 1s spectra have three overlapping peaks, indicating that the oxygen is presents at several states, including OM, OH^-, and H_2O. The OM refers to metal oxides in the passive film, and the OH^- ion is hydroxyl oxygen which is related to protons in the passive film. Besides, H_2O refers to the absorbed water in the passive film. It should be noted that the fraction of H_2O in oxide film is relatively low due to the dehydration effect in the air [51]. Moreover, the

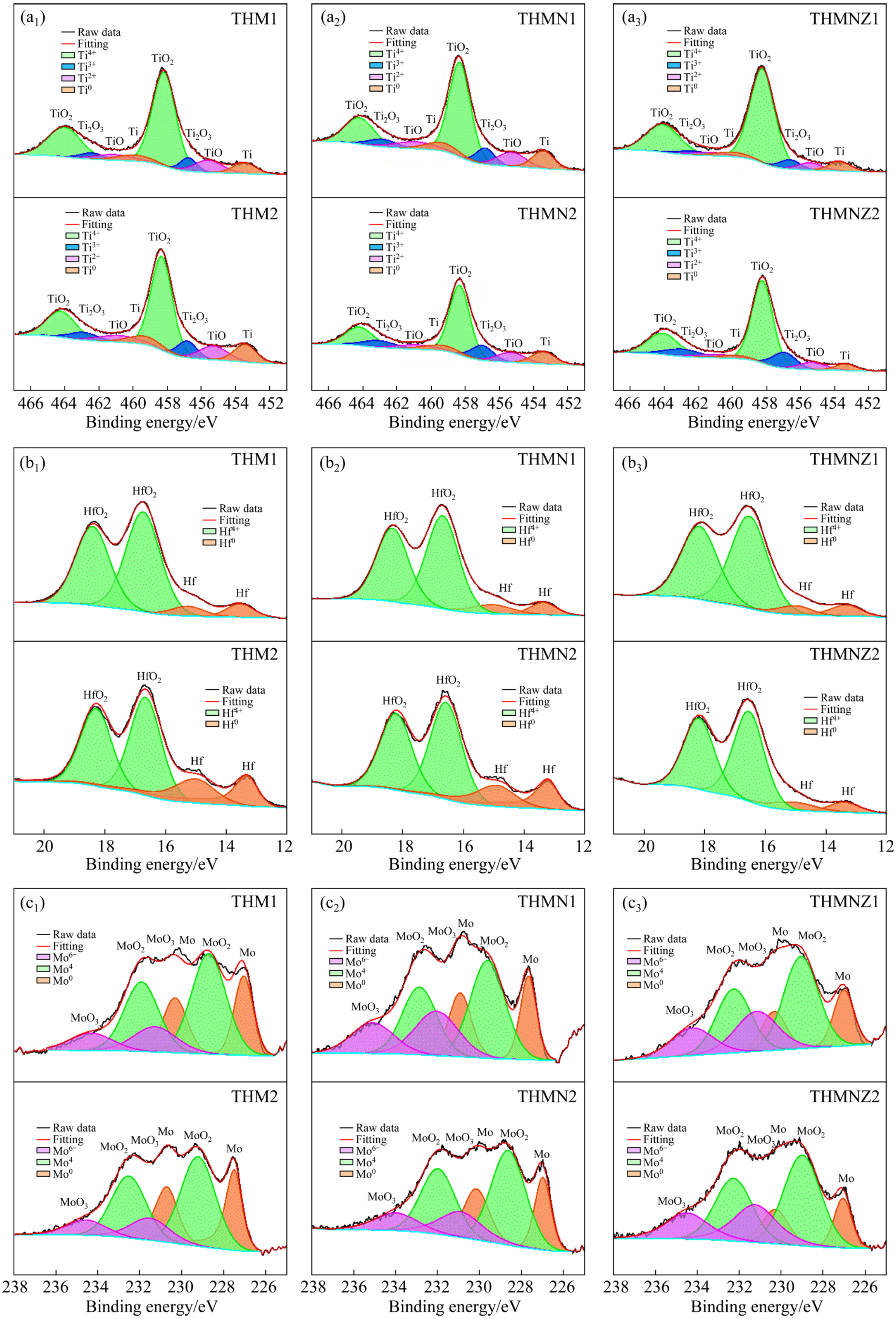

Fig. 8 Deconvoluted high-resolution XPS spectra for Ti 2p (a_1−a_3), Hf 4f (b_1−b_3), and Mo 3d (c_1−c_3) of MPEAs after being immersed in SBF solution for 24 h

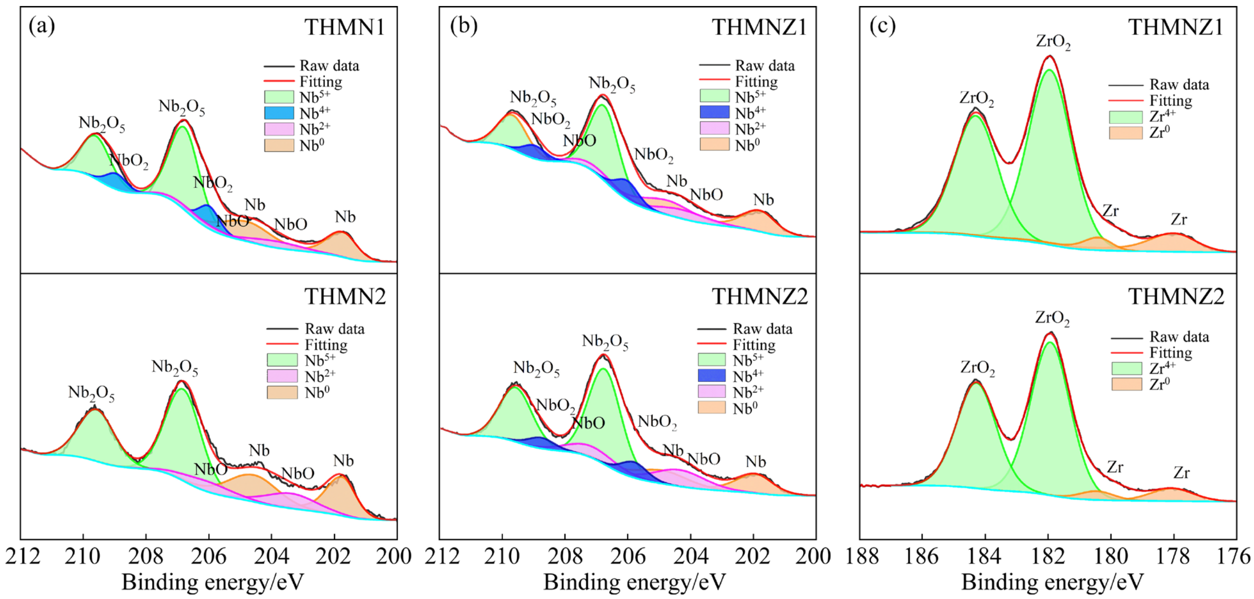

Fig. 9 Deconvoluted high-resolution XPS spectra for Nb 3d (a, b) and Zr 3d (c) of MPEAs after being immersed in SBF solution for 24 h

content of metal oxides in THM2 (39.81%) and THMN2 (38.16%) alloys is relatively low, which is unfavorable to the microscopic uniformity and pitting resistance of the passive film on the surface of titanium alloys in Fig. 10(d).

To see the relative distribution of the oxidation states of Ti, Mo and Nb elements, stacking histograms of sub-oxide content in passive films are presented in Fig. 11. Compared with THM2 alloy, the addition of Nb and Zr reduces the content of Ti sub-oxides of THMN1, THMNZ1 and THMNZ2 alloys, which may be attributed to the growth of the stable passive films of the alloys [52]. However, it is worth mentioning that the proportion of Ti sub-oxides in THMN2 alloy is relatively high on the surface, which may be due to the large grain size and the element segregation. For the MPEAs, the elemental segregation might promote the formation of less stable oxides, and the dendritic and inter-dendritic regions with different compositions may also create a potential difference, resulting in a galvanic reaction between the two regions in the MPEAs [53]. In contrast to the high valence oxides of Ti and Nb, the surface stable MoO_2 of MPEAs has a relatively low content. Moreover, the addition of Nb and Zr reduces the relative content of MoO_3 in the passive films, which may be attributed to the preferential formation of stable oxides of Nb and Zr.

The multi-element composition of MPEA leads to the film formation of multiple elements competing on the alloy surface. From the perspective of thermodynamic, the driving force for the formation of the passive films on the MPEAs can be expressed in terms of the Gibbs free energy ($\Delta_r G_m^{\ominus}$) of the reaction of the metal with solution. Since the formation of oxides in air and aqueous solutions is different, it should be noted that the order of preferential oxidation of different metal elements does not simply follow the magnitude of the $\Delta_r G_m^{\ominus}$, and the environment also has an impact on the formation capacity of oxides. Moreover, oxide formation occurs at the oxide−solution (o−s) and metal−oxide (m−o) interfaces. The definition of $\Delta_r G_m^{\ominus}$ and the reaction conditions in aqueous solution are different due to the different availability of oxidants. In this sense, it is necessarily normalized by real reactants, case by case. Taking the preceding consecutive reaction of Nb element as an example (Eqs. (9)−(11)), when the oxidizing agent is sufficient in supply and the oxide formation occurs at the o−s interface, the total reaction can be expresses as

$$\mathrm{Nb+5/2H_2O=1/2Nb_2O_5+5H^++5e} \tag{12}$$

In contrast, when the O^{2-} ion is insufficient in supply, the total reaction at the m−o interface is expressed as

$$\mathrm{2/5Nb+H_2O=1/5Nb_2O_5+2H^++2e} \tag{13}$$

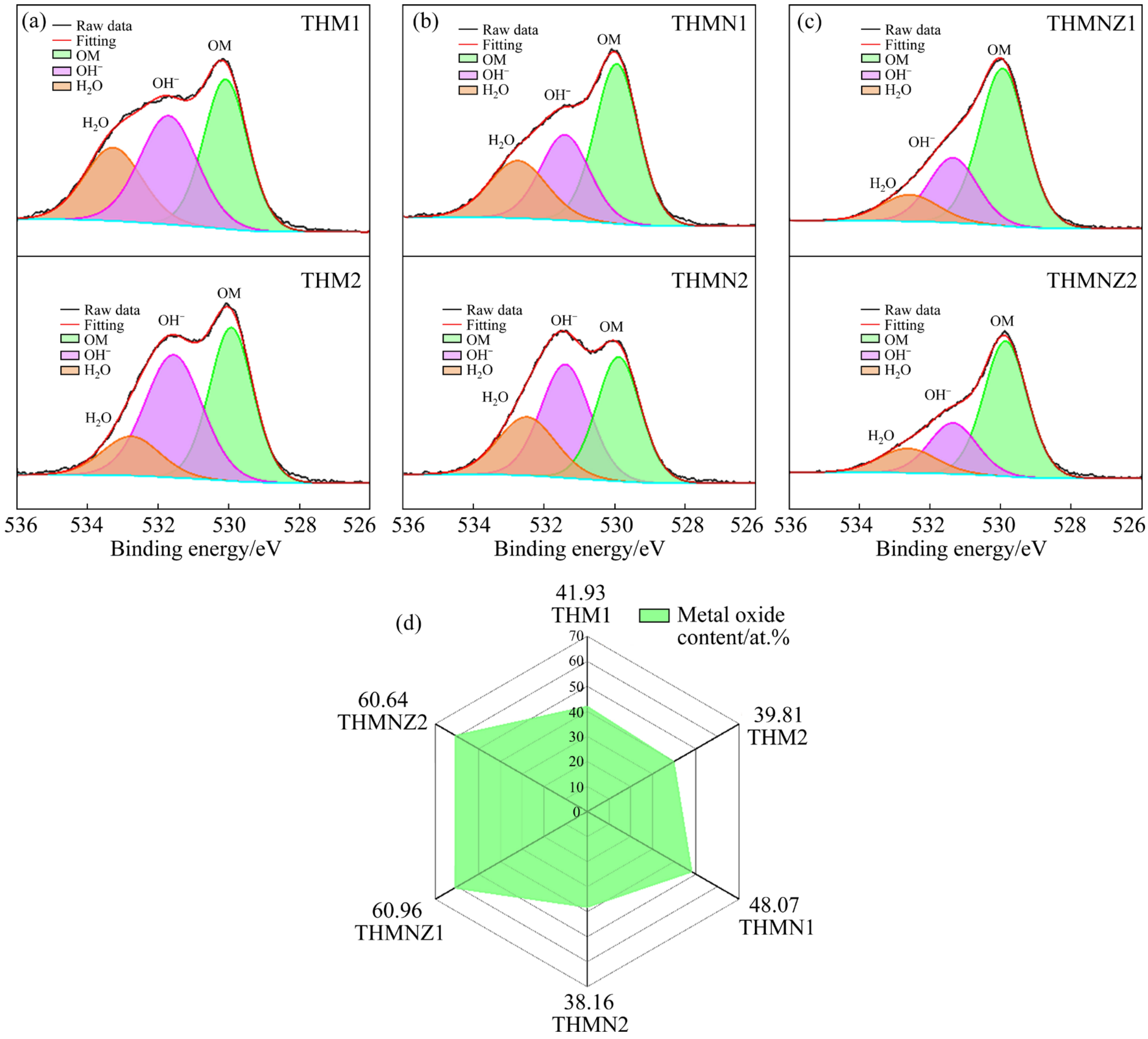

Fig. 10 Deconvoluted high-resolution XPS spectra for O 1s (a−c) and content of metal oxides in passive film (d) of MPEAs after being immered in SBF solution for 24 h

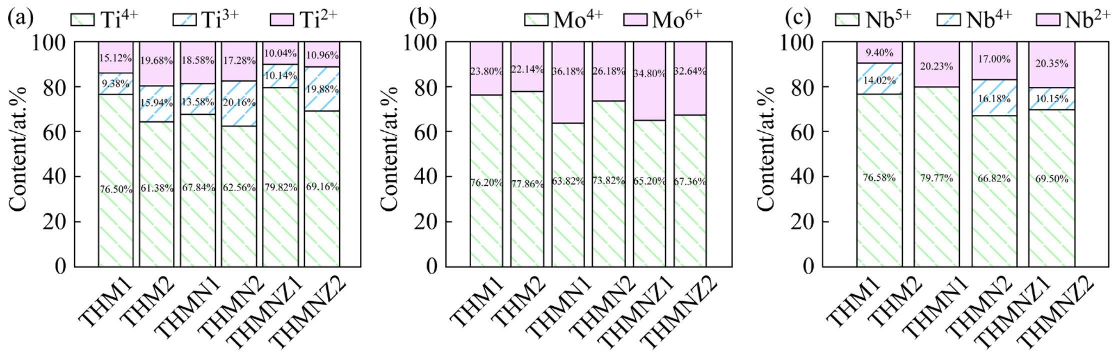

Fig. 11 Stacking histograms of sub-oxide content in passive films: (a) Ti 2p; (b) Mo 3d; (c) Nb 3d

The $\Delta_r G_m^\ominus$ of Reactions (12) and (13) is respectively calculated as −290.05 and −116.02 kJ/mol. For the sake of comparison, all relevant data for the different elements are listed in Table 8, where $\Delta_{r1} G_m^\ominus$ represents Gibbs free energy change of the oxide formation occurring at the o−s interface, and $\Delta_{r2} G_m^\ominus$ represents Gibbs free energy change of the oxide formation occurring at the m−o interfaces. Then, the order in which each metal element forms the main stable oxides is as follows: $HfO_2 > ZrO_2 >$

$TiO_2 > Nb_2O_5 > MoO_2$. The cationic concentrations in the surface films of the MPEAs immersed in SBF solution are displayed in Fig. 12, and the contents of oxides are listed in Table 9. Comparing the nominal composition of the MPEAs, the contents of Hf and Zr are higher than those in the substrate, and the content of Ti is somewhat higher than that in the substrate. On the contrary, the contents of Nb and Mo are lower than those in the substrate. Therefore, the elements of Hf, Zr, and Ti in the MPEAs are more susceptible to oxidation, resulting in the formation of stable oxides. The preferred oxides dominated by thermodynamic factors are in agreement with the XPS results except THMNZ1 and THMNZ2 alloys. Besides, when the O^{2-} ion is insufficient in supply obviously, the oxidation state of Nb is more likely to be NbO instead of NbO_2 (NbO ($\Delta_{r2}G_m^\ominus$)<NbO_2 ($\Delta_{r2}G_m^\ominus$)). This may also be the reason why NbO is present in the passive film without the presence of NbO_2 for THMN1 alloy.

Table 8 Standard Gibbs free energy of formation ($\Delta_f G_m^\ominus$) of associated oxides, Gibbs free energy change ($\Delta_{r1} G_m^\ominus$) of oxide formation occurring at o−s interfaces and Gibbs free energy change ($\Delta_{r2} G_m^\ominus$) of oxide formation occurring at m−o interfaces

Species	$\Delta_f G_m^\ominus$/ (kJ·mol^{-1})	$\Delta_{r1} G_m^\ominus$/ (kJ·mol^{-1})	$\Delta_{r2} G_m^\ominus$/ (kJ·mol^{-1})
TiO_2	−1434.2	−414.52	−207.26
Ti_2O_3	−888.8	−361.39	−240.93
TiO	−495.0	−257.86	−257.86
HfO_2	−1088.2	−613.92	−306.96
MoO_3	−668.1	43.32	14.44
MoO_2	−533.0	−58.77	−29.36
Nb_2O_5	−1765.8	−290.05	−116.02
NbO_2	−740.5	−266.22	−133.11
NbO	−392.6	−155.46	−155.46
ZrO_2	−1042.8	−568.52	−284.26
H_2O	−237.14	−	−

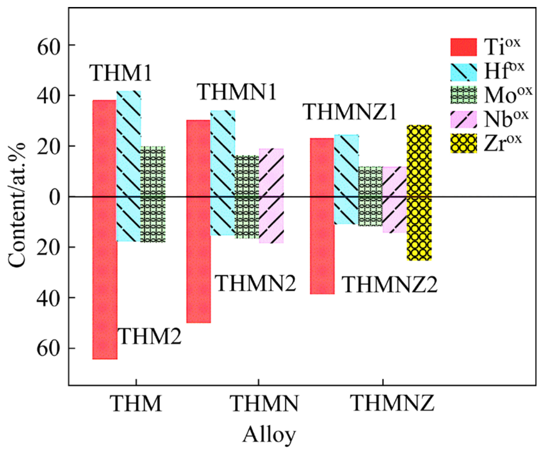

Fig. 12 Oxide content of passive films formed on MPEAs (ox: Oxidized state)

It is noticeable that ZrO_2 has a higher preferential oxidation degree than HfO_2 for THMNZ1 and THMNZ2 alloys, and that is contrary to the oxide formation sequence dominated by thermodynamic parameters (HfO_2<ZrO_2). This result is mainly due to the fact that the migration of metallic cations and oxide anions within the passive film is the other factor to affect the oxide species in passive film on the alloy [54]. The migration rate of ions can be defined as the ratio of the current density contributed by the metal cation migration in the reaction to the total ion current density, which is related to the metal−oxygen binding bond energy, ionic radius and dielectric constant, and its value can be reflected by n_M [54,55]. For the THMNZ1 and THMNZ2 alloys, the n_M of Hf and Zr is about 0.05 and 0.09, respectively, which indicates that Zr has the large ion migration rate [56,57]. Moreover, it is reported that high contents of Ti and Nb dominate the amorphous properties of the oxide film, and enhance the movement of Zr^{4+} ions, resulting in a higher content of Zr than that of Hf in the passive film [58].

3.7 Surface wettability

Typically, the wettability can be reflected by the contact angle. Thus, the contact angle is recorded by sessile drop through the dropping of SBF solution from a syringe onto the surface of the samples. Figure 13 shows the photographs taken from the samples and the corresponding average contact angels. In the figure, CP-Ti has the smallest contact angle of (57.5±0.8)° and THM1 alloy has the largest contact angle of (74.4±1.0)°. The contact angles of MPEAs are within the range of 65°−75°, which may be caused by the dense lattice structure of BCC structure [59]. Compared with CP-Ti and Ti6Al4V alloy, the Ti-based BCC MPEAs contain higher volume fraction of BCC phase, and the dense lattice structure of BCC Ti alloy increases the electron density on the alloy surface, reduces the surface energy of the alloy, and thus makes the liquid form a larger contact angle on the alloy

Table 9 Cationic fractions of surface films on MPEAs immersed in SBF solution

Alloy	Content/at.%									
	Ti^{4+} (TiO_2)	Ti^{3+} (Ti_2O_3)	Ti^{2+} (TiO)	Hf^{4+} (HfO_2)	Mo^{6+} (MoO_3)	Mo^{4+} (MoO_2)	Nb^{5+} (Nb_2O_5)	Nb^{4+} (NbO_2)	Nb^{2+} (NbO)	Zr^{4+} (ZrO_2)
THM1	29.2	3.58	5.4	41.9	4.72	15.2	−	−	−	−
THM2	43.68	8.75	11.95	17.52	4.02	14.08	−	−	−	−
THMN1	17.9	9.84	2.74	34.12	5.94	10.48	13.78	3.04	2.16	−
THMN2	31.57	10.16	8.31	15.12	4.3	12.1	14.72	−	3.72	−
THMNZ1	19.31	2.02	1.93	24.56	4.1	7.7	8.02	2.04	1.92	28.4
THMNZ2	26.64	7.67	4.23	10.68	3.76	7.72	9.87	1.44	2.89	25.1

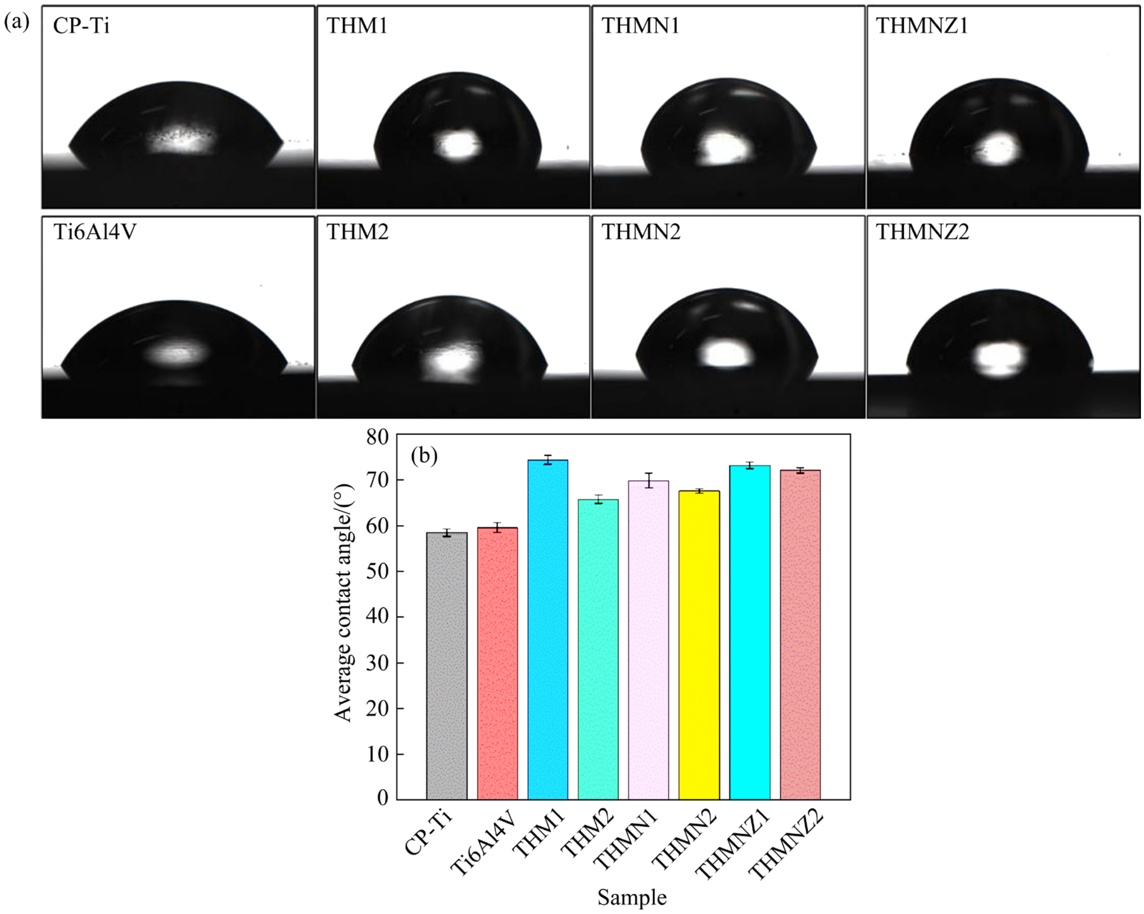

Fig. 13 Photographs (a) and average contact angles (b) of samples

surface. In addition, a larger contact angle usually means that the surface is more hydrophobic. The corrosion resistance of alloy is also closely related to hydrophobicity and hydrophilia, and a hydrophobic surface generally brings about high corrosion resistance in a metal [60]. Therefore, the THM1, THMN1, THMNZ1 and THMNZ2 alloys present large contact angles in SBF solution, exhibiting excellent corrosion resistance. Furthermore, the contact angle is an important parameter for implant biomaterials, which is associated with a series of biological reactions such as protein adsorption, activation of blood coagulation and bioadhesion [61]. The contact angle of the surface is less than 90° for most hydrophilic materials. According to the report that cells tend to adhere onto surfaces with a water contact angle of approximately 70° [62], all MPEAs possess surface hydrophilicity intrinsically, and their surface contact angles are beneficial to cell adhesion and attachment, which have good potential for biomedical applications.

4 Conclusions

(1) All MPEAs after the solution annealing have a single BCC phase structure without any intermetallic compounds. The average grain size of equimass TiHfMo and TiHfMoNb alloys is 250−300 μm, while that of the other MPEAs is less than 250 μm. The small average grain size of equiatomic refractory alloys indicates that the sluggish diffusion occurs in the MPEAs.

(2) The hardness and Young's moduli of MPEAs are within the range of 5.5−6.4 and 95.6−126.2 GPa, respectively. The ratios of H/E and H^3/E^2 for MPEAs are respectively larger than 0.04 and 0.009, enabling better wear resistance.

(3) The passive films are composed of a bi-layered microstructure and the corrosion process of Ti substrate is hindered mainly by the inner film. According to the potentiodynamic polarization curves and EIS analysis, the corrosion resistance of MPEAs is as follows: THM1 > THMN1 > Ti6Al4V > THMNZ2 > CP-Ti > THMNZ1 > THM2 > THMN2. Mott−Schottky analysis presents n-type semiconducting characteristics for all the passive films formed on the MPEAs. Moreover, these passive films have high resistance to Cl^- ions attack.

(4) XPS results show that a variety of stable oxides such as TiO_2, HfO_2, MoO_2, Nb_2O_5 and ZrO_2 are formed on the surface of the MPEAs. Moreover, the growth rates of ZrO_2 and MoO_2 are respectively the highest and lowest, the rate of HfO_2 is lower than that of ZrO_2, and TiO_2 has a higher growth rate than Nb_2O_5. The present results are supported by thermodynamic calculations and kinetic analysis.

(5) The MPEAs possess larger contact angles than CP-Ti and Ti6Al4V alloy, exhibiting excellent corrosion resistance.

CRediT authorship contribution statement

Hao-qin LIN: Investigation, Formal analysis, Writing; **Pan REN:** Investigation, Visualization; **Guang-xu ZHANG:** Investigation; **Wei-min CHEN:** Supervision, Conceptualization, Writing − Review & editing, Project administration, Funding acquisition; **Li-jun ZHANG:** Formal analysis, Writing − Review & editing.

Declaration of competing interest

The authors declare that they have no known competing financial interests or personal relationships that could have appeared to influence the work reported in this paper.

Data availability

All the data included in this article are available upon request by contact the corresponding author.

Acknowledgments

The authors gratefully acknowledge the financial supports from the National Key Research and Development Program of China (No. 2022YFB3707501), the National Natural Science Foundation of China (No. 51701083), and GDAS' Project of Science and Technology Development, China (Nos. 2022GDASZH-2022010103, 2022GDASZH-2022010107, 2020GDASYL-20200102030). Pan REN acknowledges the financial support from the National Natural Science Foundation of China (No. 52001137), and the Basic and Applied Basic Research Foundation of Guangzhou, China (No. 202201010206).

References

[1] CHEN Qi-zhi, THOUAS G A. Metallic implant biomaterials [J]. Materials Science and Engineering: R, 2015, 87: 1−57.

[2] DAVIS R, SINGH A, JACKSON M J, COELHO R T, PRAKASH D, CHARALAMBOUS C P, AHMED W, DA SILVA L R R, LAWRENCE A A. A comprehensive review on metallic implant biomaterials and their subtractive manufacturing [J]. The International Journal of Advanced Manufacturing Technology, 2022, 120: 1473−1530.

[3] ZHANG Yi-ning, YANG Hai-Lin, JUAIM A N, CHEN Xiao-na, LU Chang, ZOU Ling, WANG Yin-zhou, ZHOU Xiong-wen. Biocompatibility and osteogenic activity of Zr-30Ta and Zr−25Ta−5Ti sintered alloys for dental and orthopedic implants [J]. Transactions of Nonferrous Metals Society of China, 2023, 33: 851−864.

[4] MILOŠEV I. Metallic materials for biomedical applications: Laboratory and clinical studies [J]. Pure and Applied Chemistry, 2011, 83: 309−324.

[5] LI Qiang, HUANG Qi, LI Jun-jie, HE Qian-feng, NAKAI M, ZHANG Ke, NIINOMI M, YAMANAKA K, CHIBA A, NAKANO T. Microstructure and mechanical properties of Ti−Nb−Fe−Zr alloys with high strength and low elastic modulus [J]. Transactions of Nonferrous Metals Society of China, 2022, 32: 503−512.

[6] JAMARI J, AMMARULLAH M I, SANTOSO G, SUGIHARTO S, SUPRIYONO T, PRAKOSO A T, BASRI H, VAN DER HEIDE E. Computational contact pressure prediction of CoCrMo, SS 316L and Ti6Al4V femoral head against UHMWPE acetabular cup under gait cycle [J]. Journal of Functional Biomaterials, 2022, 13: 64.

[7] RAO S, USHIDA T, TATEISHI T, OKAZAKI Y, ASAO S. Effect of Ti, Al, and V ions on the relative growth rate of fibroblasts (L929) and osteoblasts (MC3T3-E1) cells [J]. Bio-Medical Materials and Engineering, 1996, 6: 79−86.

[8] MIURA K, YAMADA N, HANADA S, JUNG T K, ITOI E. The bone tissue compatibility of a new Ti−Nb−Sn alloy with a low Young's modulus [J]. Acta Biomaterialia, 2011, 7: 2320−2326.

[9] LING Jin-feng, HUANG Dan-dan, BAI Ke-wu, LI Wei, YU Zhen-tao, CHEN Wei-min. High-throughput development and applications of the compositional mechanical property map of the β titanium alloys [J]. Journal of Materials Science & Technology, 2021, 71: 201−210.

[10] LIN Hao-qin, LING Jin-feng, CHEN Wei-min, WANG Yao, WU Xiao-ke, ZHANG Li-jun. High-throughput determination of mechanical and diffusion properties of Ti−Ta−Fe alloys [J]. Transactions of Nonferrous Metals Society of China, 2022, 32: 3963−3972.

[11] LIN Hao-qin, HUANG Jia-jian, CHEN Wei-min, ZHANG Li-jun. High-throughput determination of mechanical and diffusion properties in the Ti−Nb−Fe alloys [J]. Calphad, 2022, 79: 102497.

[12] WEN Zhu-hao, WANG Yao, CHEN Wei-min, ZHANG Li-jun, DU Yong. Investigation of mechanical and diffusion properties in bcc Ti−Nb−Zr−Sn alloys via a high-throughput method [J]. Transactions of Nonferrous Metals Society of China, 2021, 31: 3405−3415.

[13] LIN Hao-qin, LING Jin-feng, CHEN Wei-min. Experimental investigations on the interdiffusion behaviors and mechanical properties of Ti-rich Ti−Mo−Zr system by using the diffusion couple technique [J]. Journal of Phase Equilibria and Diffusion, 2022, 43: 448−457.

[14] YEH J W, CHEN S K, LIN S J, GAN J Y, CHIN T S, SHUN T T, TSAU C H, CHANG S Y. Nanostructured high-entropy alloys with multiple principal elements: Novel alloy design concepts and outcomes [J]. Advanced Engineering Materials, 2004, 6: 299−303.

[15] GEORGE E P, RAABE D, RITCHIE R O. High-entropy alloys [J]. Nature Reviews Materials, 2019, 4: 515−534.

[16] DING Ji-li, XU Hong-jie, LI Xuan, LIU Man, ZHANG Tao. The similarity of elements in multi-principle element alloys based on a new criterion for phase constitution [J]. Materials & Design, 2021, 207: 109849.

[17] LI Wei-dong, XIE Di, LI Dong-yue, ZHANG Yong, GAO Yan-fei, LIAW P K. Mechanical behavior of high-entropy alloys [J]. Progress in Materials Science, 2021, 118: 100777.

[18] SHI Yun-zhu, YANG Bing, LIAW P K. Corrosion-resistant high-entropy alloys: A review [J]. Metals, 2017, 7: 43.

[19] WANG Hao, CHEN Wei-ping, HAO Liang-yan, CHU Chen-liang, XIONG Wei, FU Zhi-qiang. Mechanical and corrosion properties of lightweight $(Ti_{60}Cr_{30}Nb_{10})_{100-x}Al_x$ medium-entropy alloys [J]. Transactions of Nonferrous Metals Society of China, 2024, 34: 219−235.

[20] LAI Wei-Ji, VOGEL F, ZHAO Xue-yang, WANG Bin-bin, YI Yan-liang, YOU De-qiang, TONG Xin, LI Wei, YU Xiang, WANG Xiao-jian. Design of BCC refractory multi-principal element alloys with superior mechanical properties [J]. Materials Research Letters, 2022, 10: 133−140.

[21] TIAN Yu-sheng, ZHOU Wen-zhe, TAN Qing-biao, WU Ming-xu, QIAO Shen, ZHU Guo-liang, DONG An-ping, SHU Da, SUN Bao-de. A review of refractory high-entropy alloys [J]. Transactions of Nonferrous Metals Society of China, 2022, 32: 3487−3515.

[22] HUSSEIN M, ADESINA A Y, KUMAR M, AZEEM M, SOROUR A, AL-AQEELI N. Improvement of in vitro corrosion, wear, and mechanical properties of newly developed Ti alloy by thermal treatment for dental applications [J]. Transactions of Nonferrous Metals Society of China, 2021, 31: 952−966.

[23] WANG Ze-ning, YAN Yu, WU Yuan, HUANG Xin, ZHANG Yi, SU Yan-jing, QIAO Li-jie. Corrosion and tribocorrosion behavior of equiatomic refractory medium entropy TiZr(Hf,Ta,Nb) alloys in chloride solutions [J]. Corrosion Science, 2022, 199: 110166.

[24] WONG K K, HSU H C, WU S C, HO W F. Structure and properties of Ti-rich Ti−Zr−Nb−Mo medium-entropy alloys [J]. Journal of Alloys and Compounds, 2021, 868: 159137.

[25] CHEN Geng-biao, YAN Hong-wei, WANG Zhe, WANG Kai-ming, YVES N I, TONG Yong-gang. Effects of Mo content on the microstructure and mechanical properties of $TiNbZrMo_x$ high-entropy alloys [J]. Journal of Alloys and Compounds, 2023, 930: 167373.

[26] YUAN Xiao-yuan, WU Yuan, ZHOU Mei-sa, LIU Xiong-jun, WANG Hui, JIANG Sui-he, ZHANG Xiao-bing, WU Hong-hui, LIU Xiao-chun, CHEN Zi-pan, XU Xiang-qi, LU Zhao-ping. Effects of trace elements on mechanical properties of the TiZrHfNb high-entropy alloy [J]. Journal of Materials Science & Technology, 2023, 152: 135−147.

[27] LI Tian-xin, WANG Shu-dao, FAN Wen-xue, LU Yi-ping, WANG Tong-ming, LI Ting-ju, LIAW P K. CALPHAD-aided design for superior thermal stability and mechanical behavior in a TiZrHfNb refractory high-entropy alloy [J]. Acta Materialia, 2023, 246: 118728.

[28] MOTALLEBZADEH A, PEIGHAMBARDOUST N S, SHEIKH S, MURAKAMI H, GUO S, CANADINC D. Microstructural, mechanical and electrochemical characterization of TiZrTaHfNb and $Ti_{1.5}ZrTa_{0.5}Hf_{0.5}Nb_{0.5}$ refractory high-entropy alloys for biomedical applications [J]. Intermetallics, 2019, 113: 106572.

[29] KUMAR P, JAIN N K, JAISWAL S, GUPTA S. Development of Ti−Ta−Nb−Mo−Zr high entropy alloy by μ-plasma arc additive manufacturing process for knee implant applications and its biocompatibility evaluation [J]. Journal of Materials Research and Technology, 2023, 22: 541−555.

[30] GUO N N, WANG L, LUO L S, LI X Z, SU Y Q, GUO J J, FU H Z. Microstructure and mechanical properties of refractory MoNbHfZrTi high-entropy alloy [J]. Materials & Design, 2015, 81: 87−94.

[31] SENKOV O N, SCOTT J M, SENKOVA S V, MIRACLE D B, WOODWARD C F. Microstructure and room temperature properties of a high-entropy TaNbHfZrTi alloy [J]. Journal of Alloys and Compounds, 2011, 509: 6043−6048.

[32] ZHANG Yong, ZHOU Yun-jun, LIN Jun-pin, CHEN Guo-liang, LIAW P K. Solid-solution phase formation rules for multi-component alloys [J]. Advanced Engineering Materials, 2008, 10: 534−538.

[33] ZHANG Y, YANG X, LIAW P K. Alloy design and properties optimization of high-entropy alloys [J]. JOM, 2012, 64: 830−838.

[34] FANG Shou-shi, XIAO Xue-shan, XIA Lei, LI Wei-huo, DONG Yuan-da. Relationship between the widths of

supercooled liquid regions and bond parameters of Mg-based bulk metallic glasses [J]. Journal of Non-Crystalline Solids, 2003, 321: 120−125.

[35] LI Zhen, LAI Wei-ji, WANG Bin-bin, TONG Xin, YOU De-qiang, LI Wei, WANG Xiao-jian. A novel $Ti_{42.5}Zr_{42.5}Nb_5Ta_{10}$ multi-principal element alloy with excellent properties for biomedical applications [J]. Intermetallics, 2022, 151: 107731.

[36] TSAI K Y, TSAI M H, YEH J W. Sluggish diffusion in Co−Cr−Fe−Mn−Ni high-entropy alloys [J]. Acta Materialia, 2013, 61: 4887−4897.

[37] CHEN Wei-min, ZHANG Li-jun. High-throughput determination of interdiffusion coefficients for Co−Cr−Fe−Mn−Ni high-entropy alloys [J]. Journal of Phase Equilibria and Diffusion, 2017, 38: 457−465.

[38] LEYLAND A, MATTHEWS A. On the significance of the H/E ratio in wear control: A nanocomposite coating approach to optimised tribological behaviour [J]. Wear, 2000, 246: 1−11.

[39] BALYANOV A, KUTNYAKOVA J, AMIRKHANOVA N A, STOLYAROV V V, VALIEV R Z, LIAO X Z, ZHAO Y H, JIANG Y B, XU H F, LOWE T C, ZHU Y T. Corrosion resistance of ultra fine-grained Ti [J]. Scripta Materialia, 2004, 51: 225−229.

[40] JIN Lei, CUI Wen-fang, SONG Xiu, LIU Gang, ZHOU Lian. Effects of surface nanocrystallization on corrosion resistance of β-type titanium alloy [J]. Transactions of Nonferrous Metals Society of China, 2014, 24: 2529−2535.

[41] EISENBARTH E, VELTEN D, MÜLLER M, THULL R, BREME J. Biocompatibility of beta-stabilizing elements of titanium alloys [J]. Biomaterials, 2004, 25: 5705−5713.

[42] TANJI A, FAN X S, SAKIDJA R, LIAW P K, HERMAWAN H. Niobium addition improves the corrosion resistance of $TiHfZrNb_x$ high-entropy alloys in Hanks' solution [J]. Electrochimica Acta, 2022, 424: 140651.

[43] HSU C H, MANSFELD F. Concerning the conversion of the constant phase element parameter Y0 into a capacitance [J]. Corrosion, 2001, 57: 747−748.

[44] JAYARAJ J, SHANKAR A R, MUDALI U K. Electrochemical and passive characterization of a beta type $Ti_{45}Zr_{38}Al_{17}$ cast rod in nitric acid medium [J]. Electrochimica Acta, 2012, 85: 210−219.

[45] HE G, ZHU L Q, LIU M, FANG Q, ZHANG L D. Optical and electrical properties of plasma-oxidation derived HfO_2 gate dielectric films [J]. Applied Surface Science, 2007, 253: 3413−3418.

[46] GAD-ALLAH A G, ABD EL-RAHMAN H A. Nature and stability of anodic oxide films formed on molybdenum in chloride solutions [J]. Journal of Applied Electrochemistry, 1988, 18: 441−446.

[47] JI Peng-fei, CHEN Bo-han, LIU Shu-guang, LI Bo, XIA Chao-qun, ZHANG Xin-yun, MA Ming-zhen, LIU Ri-ping. Controlling the mechanical properties and corrosion behavior of biomedical TiZrNb alloys by combining recrystallization and spinodal decomposition [J]. Journal of Materials Science & Technology, 2022, 110: 227−238.

[48] WAKINO K, OKADA T, YOSHIDA N, TOMONO K. A new equation for predicting the dielectric constant of a mixture [J]. Journal of the American Ceramic Society, 1993, 76: 2588−2594.

[49] LIU Hui, YANG Jun-jie, ZHAO Xue-yang, SHENG Yin-ying, LI Wei, CHANG Chi-lung, ZHANG Qiang, YU Zhen-tao, WANG Xiao-jian. Microstructure, mechanical properties and corrosion behaviors of biomedical Ti−Zr−Mo−xMn alloys for dental application [J]. Corrosion Science, 2019, 161: 108195.

[50] HIRSCHORN B, ORAZEM M E, TRIBOLLET B, VIVIER V, FRATEUR I, MUSIANI M. Determination of effective capacitance and film thickness from constant-phase-element parameters [J]. Electrochimica Acta, 2010, 55: 6218−6227.

[51] MILOŠEV I, KOSEC T, STREHBLOW H H. XPS and EIS study of the passive film formed on orthopaedic Ti−6Al−7Nb alloy in Hank's physiological solution [J]. Electrochimica Acta, 2008, 53: 3547−3558.

[52] GONZALEZ E D, GIL L V G, KUGELMEIER C L, AMIGÓ-BORRAS V, MASTELARO V R, ROVERE C A D, NASCENTE P A P. Effect of Zr content on the physicochemical, electrochemical, and biological properties of $Ti_{80}Nb_{20}$-based alloys [J]. Materials Today Communications, 2022, 32: 104069.

[53] OZDEMIR H C, NAZARAHARI A, YILMAZ B, UNAL U, MAIER H J, CANADINC D, BEDIR E, YILMAZ R. Understanding the enhanced corrosion performance of two novel Ti-based biomedical high entropy alloys [J]. Journal of Alloys and Compounds, 2023, 956: 170343.

[54] MIRZOEV R A, DAVYDOV A D, STEPANOVA N I. The effect of electrolyte anions incorporated into anodic oxide films on the experimental transport numbers of ions [J]. Electrochimica Acta, 2011, 56: 4414−4419.

[55] WANG Mei-hui, HEBERT K R. Metal and oxygen ion transport during ionic conduction in amorphous anodic oxide films [J]. Journal of the Electrochemical Society, 1999, 146: 3741−3749.

[56] FOGAZZA M, SANTAMARIA M, DI QUARTO F, GARCIA-VERGARA S J, MOLCHAN I, SKELDON P, THOMPSON G E, HABAZAKI H. Formation of anodic films on sputtering-deposited Al−Hf alloys [J]. Electrochimica Acta, 2009, 54: 1070−1075.

[57] KHALIL N, LEACH J S L. The anodic oxidation of valve metals: I. Determination of ionic transport numbers by α-spectrometry [J]. Electrochimica Acta, 1986, 31: 1279−1285.

[58] HABAZAKI H, UOZUMI M, KONNO H, SHIMIZU K, NAGATA S, ASAMI K, MATSUMOTO K, TAKAYAMA K, ODA Y, SKELDON P, THOMPSON G E. Influences of structure and composition on growth of anodic oxide films on Ti−Zr alloys [J]. Electrochimica Acta, 2003, 48: 3257−3266.

[59] XIE Fang-xia, LU Dong-xing, CAO Shu, MU Yan-ming, SUN Qi-chao. Electrochemical corrosion behavior and in vitro biocompatibility of Ti−Nb−Sn alloy for dental applications [J]. Corrosion Science, 2023, 224: 111531.

[60] JU Jiang, LI Jing-jing, JIANG Ming, LI Meng-Ya, YANG Li-Xiang, WANG Kai-ming, YANG Chao, KANG Mao-dong, WANG Jun. Microstructure and electrochemical corrosion behavior of selective laser melted Ti−6Al−4V alloy in simulated artificial saliva [J]. Transactions of Nonferrous Metals Society of China, 2021, 31: 167−177.

[61] VOGLER E A. Water and the acute biological response to surfaces [J]. Journal of Biomaterials Science: Polymer Edition, 1999, 10: 1015−1045.

[62] LIN Ji-xing, TONG Xian, SHI Zi-mu, ZHANG De-chuang, ZHANG Li-shu, WANG Kun, WEI Ai-ping, JIN Lu-fan, LIN Jian-guo, LI Yun-cang, WEN Cuie. A biodegradable Zn−1Cu−0.1Ti alloy with antibacterial properties for orthopedic applications [J]. Acta Biomaterialia, 2020, 106: 410−427.

钛基 BCC 多主元合金的显微组织、力学性能和生物腐蚀行为

林浩钦[1]，任　盼[1]，张广旭[2]，陈伟民[2]，张利军[3]

1. 暨南大学 先进耐磨蚀及功能材料研究院，广州 510632；
2. 广东省科学院 新材料研究所 国家钛及稀有金属粉末冶金工程技术研究中心
广东省金属强韧化技术与应用重点实验室，广州 510650；
3. 中南大学 粉末冶金国家重点实验室，长沙 410083

摘　要：制备等原子比和等质量比 TiHfMo、TiHfMoNb 和 TiHfMoNbZr 合金，并系统研究它们的显微组织、力学性能和生物腐蚀行为。结果表明，所有多主元合金(MPEAs)均为单一的 BCC 相结构，不含有金属间化合物。此外，多主元合金的杨氏模量和硬度分别在 95~126 GPa 和 5.5~6.4 GPa 范围内。在模拟体液中，由于钝化膜由多种氧化物组成，且表面具有较大的接触角，多主元合金具有优异的抗氯离子侵蚀能力。与 CP-Ti 和 Ti6Al4V 合金相比，等原子比 TiHfMo 和 TiHfMoNb 合金具有优良的耐点蚀和耐腐蚀性、润湿性和耐磨性的理想组合，可作为生物医用金属植入物的潜在候选材料。

关键词：多主元合金；BCC 相钛合金；显微组织；力学性能；生物腐蚀行为；钝化膜

(Edited by Xiang-qun LI)